Mixing performance in Split-And-Recombine Milli-Static Mixers-A numerical analysis

Charbel Habchi, Akram Ghanem, Thierry Lemenand, Dominique Della Valle, Hassan Peerhossaini

Version of Record: https://www.sciencedirect.com/science/article/pii/S0263876218306269
Manuscript_c99bb6997c5908b86c1f3db532ccabda

Mixing Performance in Split-And-Recombine Milli-Static Mixers - a Numerical Analysis

Charbel Habchi[1], Akram Ghanem[2], Thierry Lemenand[3], Dominique Della Valle[4], Hassan Peerhossaini[5,6,*]

[1]*Notre Dame University - Louaize, Thermofluids Research Group, P.O. Box: 72 Zouk Mikael, Zouk Mosbeh, Lebanon*

[2]*ELISA Aerospace, 48 Rue Raspail, 02100 Saint-Quentin, France*

[3]*Angers University, ISTIA, LARIS EA 7315, 49000 Angers, France*

[4]*ONIRIS, 44300 Nantes, France*

[5]*Université Paris Diderot, Sorbonne Paris Cité University - Energy Physics Group, AstroParticles and Cosmology-CNRS UMR 7164, 75013 Paris, France*

[6]*University of Western Ontario, Civil & Environmental Engineering and Mechanical &Materials Engineering, London, ON N6A 3K7, Canada*

Abstract

Very low Reynolds number laminar flow in Split-And-Recombine (SAR) static mixers is numerically investigated by using a finite volume method. In these configurations, advective chaotic flow structures are created by the passive control of the flow, mimicking the baker's transformation, through a series of flow splitting, rotations, and re-combinations that generate intertwined lamellar structures. This process leads to extra surface creation, which ultimately intensifies mass transfer. The main aim of this study is firstly to demonstrate the interest of this technique for enhancing mixing, while keeping pressure drops moderate, and secondly to optimize this type of geometry. For the latter stake, two different SARs, namely SAR1 (Gray's configuration) and SAR2 (Chen's configuration), are compared in terms of distributive and dispersive mixing and energy expenditures evaluated by the pressure drop. The enhancement

*Corresponding author: Tel.: (+33) 1 57 27 53 76
Email: hassan.peerhossaini@univ-paris-diderot.fr

effect of splitting/recombination is isolated through the comparison with a channel composed of small straight sections at right angle bends with alternate chiralities (referred as 3D-Flow), without splitting. A plain square-section channel is used as base-line reference geometry to assess the relative mixing efficiency of each configuration. Results show that the SAR technique is capable of enhancing mass transfer in creeping flows compared to non-splitting-flow mixers/exchangers, thus allowing a gain in residence time and mixer size for the same final results. Between the two SAR geometries, the superiority of Chen's configuration regarding the relative mixing efficiency is demonstrated, with 83% mixing intensification, accompanied by a cost increase of 68% in the friction coefficient.

Keywords: mixing enhancement; CFD study; static mixer; creeping flow; baker's transform.

1 Introduction

Laminar mixing is important for many engineering applications where turbulence cannot be used or generated. This is a common issue in pharmaceutical, cosmetic, and biological applications where highly viscous and fragile fluids are frequently used. In this case, mixing should be enhanced at very low Reynolds numbers without utilizing vortex generators or turbulence promoters. Compactness of mixers in laminar regime is also of great importance [1] since the mixing time, i.e. the time required for achieving a certain degree of homogeneity, is usually larger than that in turbulent flow regimes.

This challenge has led to the development and optimization of the so-called “Split And Recombine” (SAR) static mixers [2-5]. SAR mixer consists of a network of divided and then recombined channels in which several fluids are introduced separately and mixed by a multi-lamination process. This SAR topology performs a series of baker’s transforms on the concentration profile [6]. The flow stream-tubes are split out, rotated in opposite directions and then recombined, folding over the concentration profile and doubling the transvers gradient. Successive vertical separation and horizontal reuniting of fluid streams increase the number of laminates with each stage; hence the contact-surface area between the two fluids is exponentially increased, resulting in faster mixing [7, 8]. Recent investigations [6, 9, 10] revealed the chaotic nature of the SAR flow and under favorable conditions, the maximum value of Lyapunov exponent of $\ln(2)$ was recorded in the SAR static mixer designed by Gray *et al.* [2].

SAR mixers can be classified in two types: the planar or 2D mixers, and the 3D configurations. Ansari and Kim [11] investigated numerically the mixing process in unbalanced splits and cross-collisions planar circular and rhombic micro-channels for Reynolds numbers ranging from 1 to 80. They showed that the lowest mixing performance is observed in the balanced collision configurations whereas the highest mixing index was obtained in the circular micro-channels in which Dean roll-cells are generated at Reynolds numbers higher than 10. Chen *et al.* [12] studied the mixing process in staggered planar Dean vortex micromixers for Reynolds numbers ranging from 0.5 to 50. It was found that for Reynolds numbers lower than 5, diffusion is dominant over advective transport, while for Reynolds numbers higher than 10 mixing is governed by Dean roll-cells.

Anxionnaz-Minvielle *et al.* [13] studied experimentally heat transfer in three different configurations of 3D SAR static mixers and compared their efficiency to planar corrugated channels. It was found that the energy efficiency of SAR mixers increases compared to that of 2D corrugated channels with increasing viscosities, especially for Reynolds numbers lower than 50. Ghanem *et al.* [9, 14] used both numerical and experimental techniques to study the mass and heat transfer in different milli-3D SAR flow configurations for different flow regimes. Comparison of the relative mixing efficiency and the energy consumption among the different flow configurations showed that the mixer proposed by Gray *et al.* [4] is more efficient in the laminar and moderately turbulent flow regimes, for Reynolds numbers ranging from 40 to 5000 [9, 14]. From the heat transfer point of view, the SAR configuration proposed by Chen and Meiners [3] shows an advantage over the other configurations for creeping and deeply laminar flows, with Reynolds numbers between 10^{-4} and 10 [9, 14].

In the present paper, numerical simulations are conducted to analyze passive scalar mixing in different 3D SAR flow configurations for a very low Reynolds number value of 10^{-3}, based on the inlet mean flow velocity. This low Reynolds number allows to highlight the baker's transforms occurring in SAR configurations and to exhibit its effects on mixing versus the increase in the pressure drop. This analysis allows establishing a hierarchy of mixers based and their mixing efficiency and opens into an optimization process.

The paper is organized as follows: section 2 is devoted to problem description and numerical model used, the results are discussed in section 3, and finally the concluding remarks are given in section 4.

2 Problem description

2.1 Governing equations

For an incompressible, steady, Newtonian fluid, the flow is governed by the continuity (Eq. (1)) and Navier-Stokes (Eq. (2)) equations:

$$\nabla \cdot \mathbf{u} = 0 \tag{1}$$

$$\mathbf{u} \cdot \nabla \mathbf{u} = -\frac{\nabla p}{\rho} + \nu \nabla^2 \mathbf{u} \tag{2}$$

where **u** is the velocity vector, ρ and ν are respectively the density and kinematic viscosity of the working fluid, and p is the pressure.

The mixing process is analyzed by tracking a passive scalar C that will allow computing the variance destruction downstream and to characterize mixing. The mass balance should be treated in a pure convective transport to quantify the kinematic mixing. Actually, CFD simulations generate a numerical diffusion that depends on the numerical scheme, the solver, and mostly the meshing. In order to obviate numerical diffusion, we have introduced a physical diffusion coefficient α, which indeed damps the pure SAR mixing effect (but remains identical in all systems for the global mixing comparison), and could be closer to the eventual experimental results. The mass transfer equation is hence given in Eq. (3):

$$\nabla \cdot (\mathbf{u}C) = \alpha \nabla^2 C \tag{3}$$

2.2 Numerical method

The computational fluid dynamics (CFD) code ANSYS Fluent 15 [15] is used for the present simulations. It is based on an Eulerian approach to compute Navier-Stokes equations through cell-centered finite volume discretization. The flow and scalar equations are solved sequentially with double precision. Third order MUSCL scheme is used for spatial discretization of the linear momentum and mass transfer equations. Diffusion terms are central-difference and second-order accurate. Pressure-velocity coupling is achieved by the SIMPLE algorithm proposed by Patankar [18].

2.3 Flow configurations and operating conditions

Numerical simulations are performed for four different flow configurations summarized in Table 1: Plain straight channel, 3D-Flow, SAR1 and SAR2 geometries. All configurations have the same flow cross-sectional area. The number of units per mixer is chosen so that all configurations lead to the same residence time (defined by the reactive volume over the flow rate ratio). For each configuration, pre- and post-conditioners are added to attenuate the entrance and exit effects on the results and to obtain a fully developed flow at the inlet of the mixer elements.

	Plain channel	3D-Flow	SAR1 [2]	SAR2 [3]
Cross section (mm^2)	3 × 3	3 × 3	3 × 3	3 × 3
Number of elements	-	18	13	10
Element developed length (mm)	-	39	54	69
Total developed length (mm)	700	702	702	690
Pre-conditioner length (mm)	-	30	30	30
Post-conditioner length (mm)	-	30	30	30

Table 1: Characteristics of the flow configurations

The first flow configuration, plain channel, is a plain straight duct of square cross section. The 3D-Flow configuration consists of a continuous duct flow with alternate bends at right angles. The two SAR configurations are referred as SAR1 and SAR2. Basic elements of the 3D-Flow, SAR1 and SAR2 configurations are shown in Figure 1. SAR1 is the geometry described by Gray *et al.* [2], we denoted this geometry SAR1 since there is one separation/recombination per element. SAR2 is the configuration described by Chen and Meiners [3], we denoted this geometry SAR2 since there are two separations/recombinations per element. Results are further normalized by those obtained in the plain square duct used as the reference geometry.

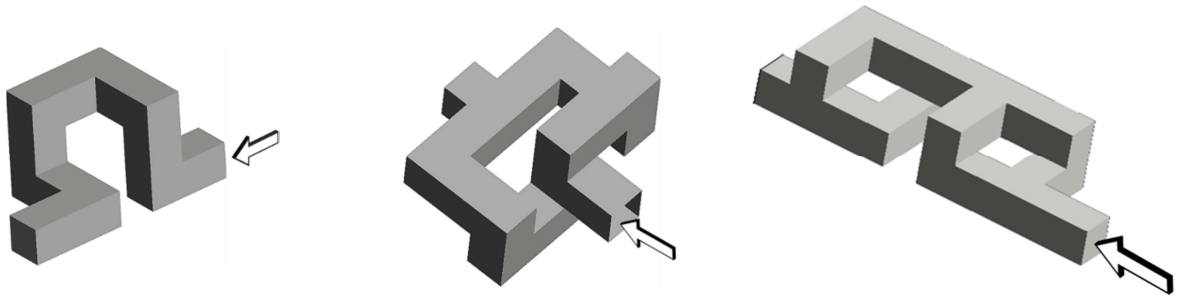

(a) (b) (c)

Figure 1: Isometric view of one element from each flow configuration: (a) 3D-Flow configuration, (b) SAR1 (Gray configuration [2]), and (c) SAR2 (Chen configuration [3])

No-slip boundary conditions are prescribed on all wall boundaries. A uniform velocity profile with average velocity equal to 3.33 cm/s is imposed at the inlet of the pre-conditioner. The scalar field at the inlet cross-section is divided into two equal parts, left and right, with $C_{left} = 0$ and $C_{right} = 1$. At the outlet, streamwise gradients of all the variables are set to zero.

The working fluid properties and operating conditions are shown in Table 2. The Reynolds number *Re*, is calculated based on the hydraulic diameter of the duct cross-section and the inlet mean flow velocity. The viscosity μ of the working fluid is chosen to match that of viscous fluid products encountered in industrial applications where SAR devices are usually used for creeping flows [19]. Numerical simulations are carried out in isothermal conditions, with a low mass diffusivity coefficient (high Péclet number) so that diffusion cannot dominate over advective mixing. In Table 2, Pe is the Péclet number representing the ratio between advective and diffusive transport rates. As noticed, the advective transport is dominant over diffusion since the diffusivity coefficient α is very small.

μ (Pa.s)	100
ρ (kg/m^3)	1000
Pe	10^6
Re	10^{-3}
α (m^2/s)	10^{-10}

Table 2: Working fluid properties and operating conditions

Scaled residual values of 10^{-8} are set as a convergence criterion for the solution of momentum and passive scalar equations.

2.4 Mesh

Since in the SAR configurations mixing elements are repeated, a series of numerical simulations were conducted for a single element in SAR1 configuration with different mesh densities in order to determine the appropriate final mesh to be used in the study. The mesh sensitivity analysis is done according to the procedure proposed by Celik *et al.* [20]; five different mesh densities were considered as shown in Table 3. The grid size ratio is the grid size of mesh $i + 1$ divided by that of mesh i; it is recommended to be at least equal to 1.3 [20]. For all cases the mesh is structured in cubical cells to reduce numerical diffusion. The criteria for the mesh sensitivity are the pressure drop, *i.e.* the pressure difference between the inlet and outlet of the SAR geometry, and the normalized standard deviation of the computed scalar value which is used to quantify mixing in the different geometries in this paper:

$$\frac{\sigma}{\sigma_0} = \frac{\sqrt{\overline{C^2} - \bar{C}^2}}{\sqrt{\overline{C_0^2} - \overline{C_0}^2}} \tag{4}$$

where $\bar{C}_0$ corresponds to the average scalar concentration at a given cross section computed in plain duct flow.

Table 3 represents the mesh sensitivity analysis performed on one element in the SAR1 configuration. As shown in this table, the value of GCI on σ/σ_0 is 0.33% and it is 0.48% for Δp for the finer mesh (mesh number 5). The GCI is similar to discretization error and could be used as error bar when presenting the results. Finally, the finer mesh 5 is adopted for all geometries.

Mesh number	1	2	3	4	5
Cell number	1.07×10^4	7.09×10^4	5.67×10^5	1.15×10^6	2.25×10^6
Grid size (mm)	0.363	0.193	0.097	0.076	0.061
Grid size ratio		1.9	2.0	1.3	1.3
σ/σ_0	0.7683	0.8373	0.9227	0.9344	0.9351
GCI_σ (%)			13.17	1.57	0.33
Δp (bar)	1.632	1.749	1.806	1.969	1.971
$GCI_{\Delta p}$ (%)			4.49	10.35	0.48

Table 3: Mesh sensitivity analysis performed on one element in the SAR1 geometry

3 Results and discussion

3.1 Flow structure

The flow streamlines through the last element in the three different geometries are shown in Figure 2. In the 3D-Flow configuration (Figure 2 (a)), the streamlines are simply twisted periodically while circulating in the successive bends. Since the flow inertial forces are small relative to the viscous forces, there is no generation of hydrodynamic instability or vortices and thus the only irreversible mixing mechanism present is the molecular diffusion. In the SAR2 configuration (Figure 2 (c)), the streamlines are evenly split into two perpendicular directions, then rotated by 90° two times before they are recombined. This process is repeated two times in each element. Here also there are no vortices or instabilities due to high fluid viscosity. However,

it will be shown later that the mixing occurs according to baker's transformation in the successive elements. The flow structure in the third configuration SAR1 (Figure 2 (b)) is somehow more complex than the first two; streamlines are initially split in two opposite directions then rotated by 90° four times in opposite directions before they are recombined together. Vortices are also absent in this configuration due to the low Reynolds number. In the next section, we examine in details how this succession of the split and recombine processes affects passive scalar mixing.

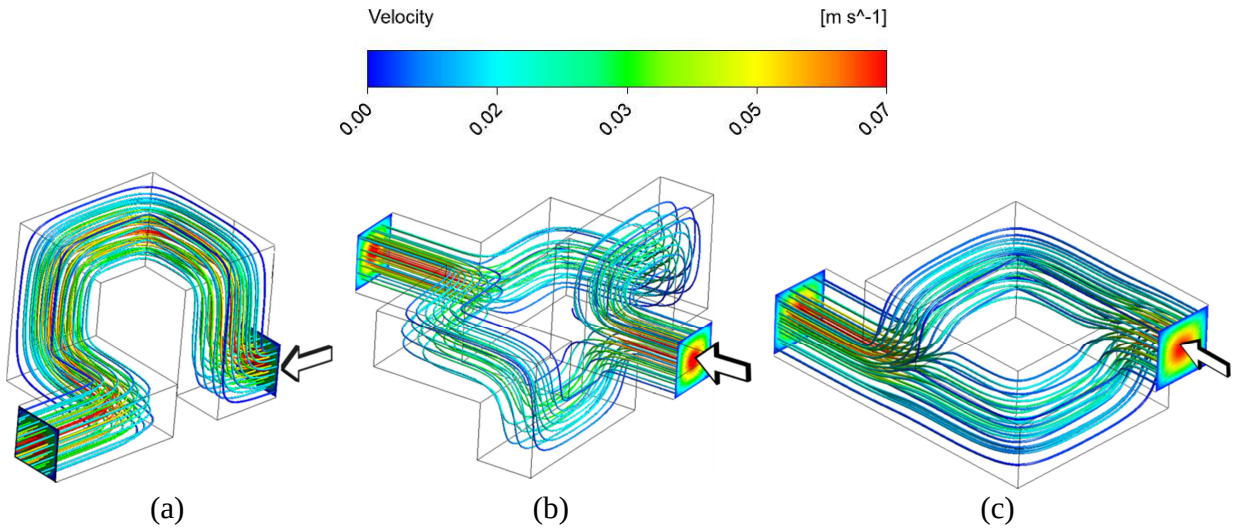

Figure 2: Streamlines through the last element of (a) 3D-Flow configuration, (b) SAR1 and (c) SAR2

3.2 Equivalent Poincaré sections and distributive mixing

Chaotic properties of the flow can be characterized by means of Poincaré sections. For this purpose, the outlet section-plane is considered for each of the four configurations. At the center of the inlet-plane, around 1000 inert particles are released starting from an initial position in the form of a disk of 0.15 mm diameter. The trajectories of the individual particles are tracked and their corresponding positions at the outlet sections are exported. The set of positions of the particles in the computational domain outlet constitute the Poincaré sections, which are shown in Figure 3. For the straight plain duct, the particles leave the outlet at the same position in which they were released at the inlet-section since the flow is laminar and the streamlines are straight. Therefore, due to high fluid viscosity and deep laminar flow, fluid particles are organized in

uniform parallel strata that move along the longitudinal direction with no radial deviation in the trajectories. Under these conditions, the 3D-Flow configuration also shows a poor dispersing performance close to the straight duct. The SAR configurations however exhibit, as expected, an effective sign of chaotic advection. The particles are laterally dispersed and are capable of visiting various radial positions in the flow cross-section, revealing the mixing enhancement by the SAR mechanism. At a first glance, the SAR2 configuration shows the best performance: particles cover the largest area of the flow cross-section and extend towards the walls, compared to SAR1 geometry in which wider gaps can be seen.

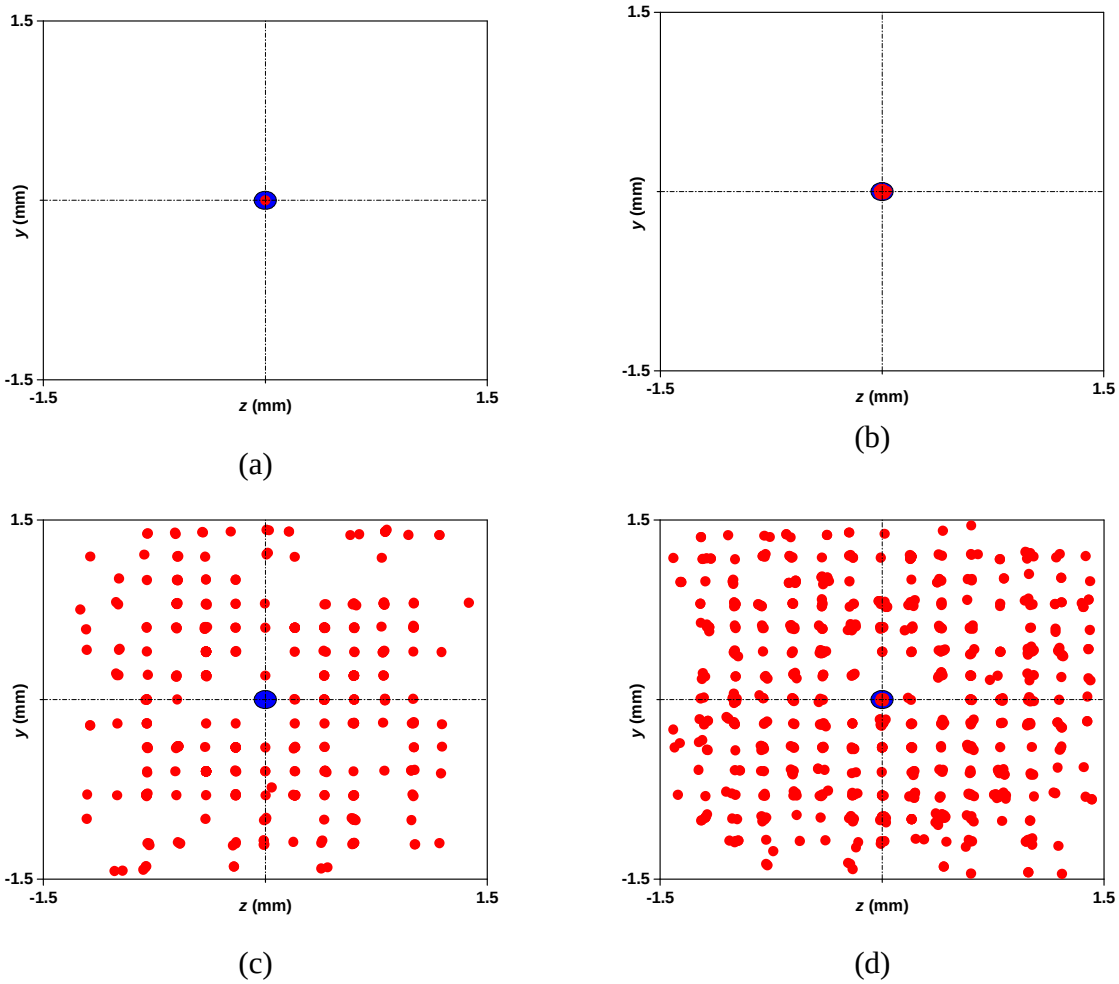

Figure 3: Poincaré sections for the studied flow configurations. The initial position is a disk (in blue) of radius 0.15 mm at the inlet center: (a) Plain channel, (b) 3D-Flow, (c) SAR1, and (d) SAR2 configurations

For a better quantitative comparison of the distributive mixing effects [21, 22], the coefficient of variation of the particle locations is computed using the radius as the characteristic length:

$$CoV_r = \frac{\sigma_r}{\bar{r}} \tag{5}$$

where $\bar{r}$ is the average radius and σ_r the standard deviation obtained as follows:

$$\sigma_r = \sqrt{\sum_{i=1}^{N} \frac{(r_i - \bar{r})^2}{N-1}} \tag{6}$$

Figure 4 compares the coefficient of variation of the distributive mixing among all the geometries studied in this work. The plain pipe represents the lowest distributive mixing performance with a CoV_r almost equal to zero. The 3D-Flow configuration comes second with a very low CoV_r, which is consistent with the Poincaré section shown in Figure 3 (b). The SAR2 geometry shows the highest performance with CoV_r around 0.347 compared to 0.299 in the SAR1 configuration, showing around 17% relative increase compared to that of the SAR1. In the next section the mixing performance is studied by the analysis of passive scalar mixing in the studied geometries.

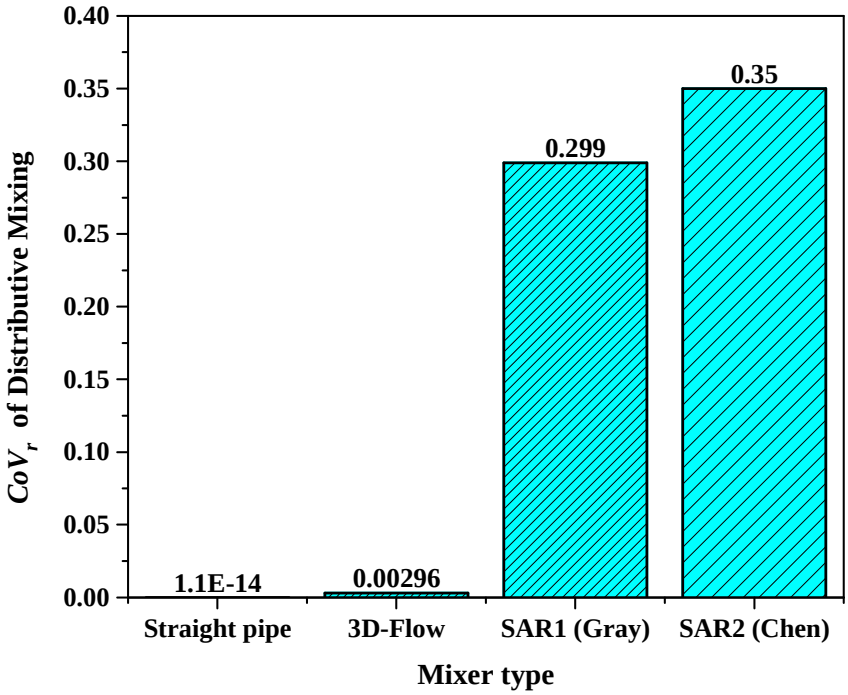

Figure 4: Distributive mixing analysis using the coefficient of variation of the particle location as characteristic distance.

3.3 Scalar mixing

Pure kinematic mixing produced by the baker's transform leads to the formation of parallel fluid layers with varying properties following the initial (inlet-section) state of segregation [6]. However, using finite volume method results in numerical diffusion due to the interpolation and discretization schemes adopted [8]. To further reduce the numerical diffusion, in addition to the mesh sensitivity analysis, we use higher order discretization schemes. Therefore a 3rd order MUSCL scheme was adopted for the convective terms in the Navier-Stokes equations.

Scalar mixing is studied by dividing the inlet-section of each configuration into two parts as shown in Figure 5 where, the left part corresponds to an arbitrary scalar value equal to 0 and the right part corresponds to a scalar value at the exit-plane of the first five elements of the 3D-Flow and the two SAR configurations. In spite of the low fluid diffusivity, with the low velocity and relatively large contact time intervals, small diffusion occurs at the interface between different scalar layers producing rather intertwined lamellar structures. Yet the signature of the SAR mechanism can be clearly detected and the arrangement of scalar strata following the theoretical predictions of the baker's transform is visible, though accompanied by the distortion caused by

molecular diffusion as shown in Figure 5 (b) and (c). From the contours in Figure 5 (a), it can be noticed that for this flow regime the bends and direction changes in the 3D-Flow configuration have no important effect on the mixing of the fluid streams. The only visible influence is that of the interfacial diffusion spreading sideways as the contact time between the different scalar layers increases downstream in the flows. By comparing qualitatively the two SAR configurations, it can be observed that the SAR2 shows a better mixing performance, where the scalar gradients are rapidly homogenized compared to SAR1 and a quasi-uniform distribution of scalar is obtained at the outlet cross-section of the fifth element.

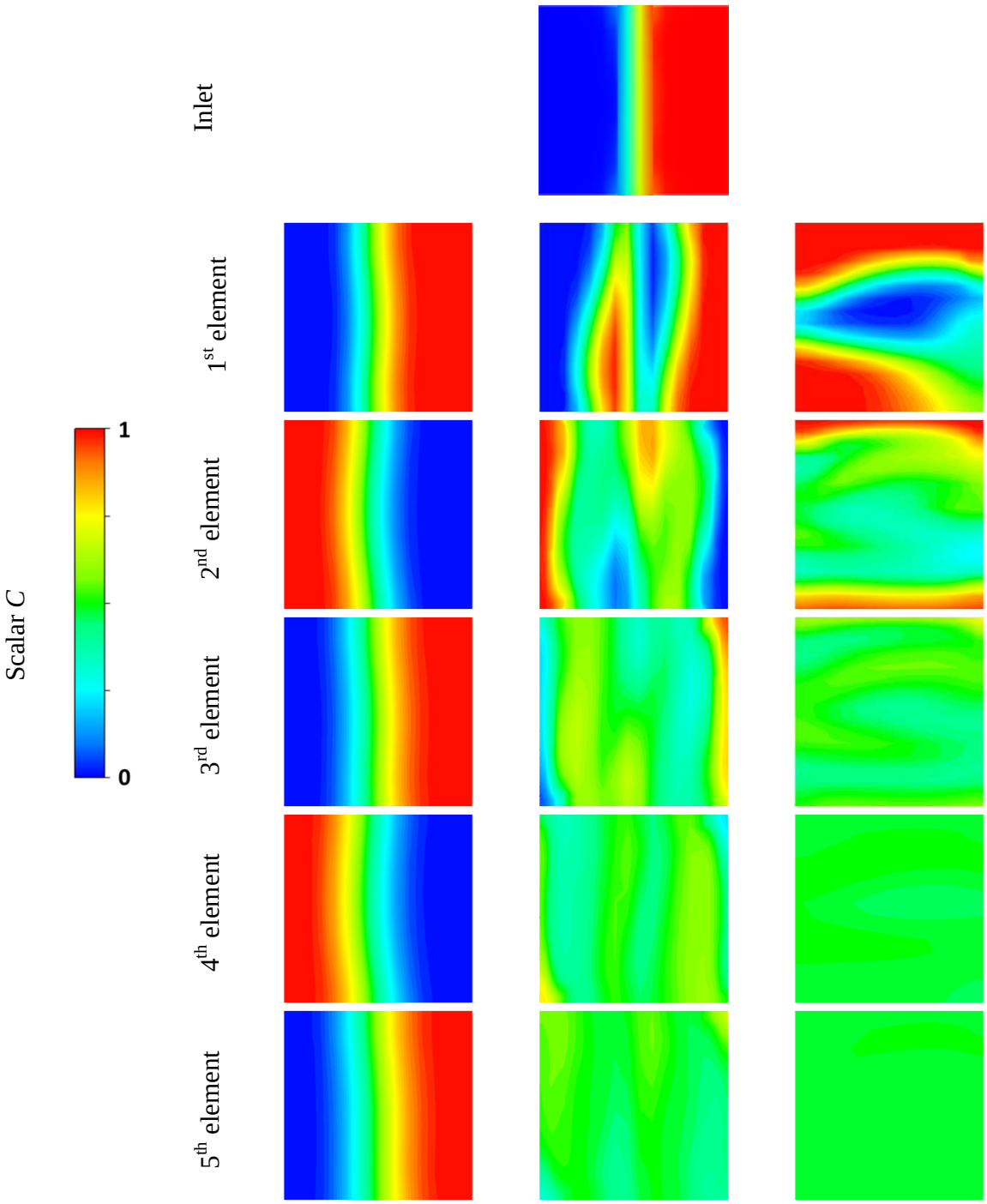

Figure 5: Scalar mixing at the outlet-section of each of the first five elements for (a) the 3D-Flow, (b) the Gray (SAR1), and (c) the Chen (SAR2) configurations.

Variation of the normalized standard deviation σ/σ_0 of the scalar at the exit of each element in the three different configurations is shown in Figure 6, plotted against the element number in Figure 6(a) and the residence length in Figure 6(b), since the elements of the different configurations do not share the same developed length. The 3D-Flow configuration shows quasi-constant levels of segregation over the entire length, with a relative standard deviation equal to 1, meaning a fully segregated state. Conversely, the segregation index decreases continuously in the SAR configurations, as the fluid flows through the different elements. As observed in the scalar distribution, SAR2 geometry clearly exhibits the best mixing quality, with a faster destruction rate than that of the SAR1 configuration. Starting from the 3rd element, the magnitude of the curve's slope increases; the gradients are rapidly dissipated by virtue of the exponential increase in the interfacial area. The exponential fitting after the 3rd element shows that the decay in σ/σ_0 for the SAR2 is almost 2.4 times greater than that in SAR1. At the inlet-section of the 5th element in SAR2 geometry, the deviation from the mean becomes inferior to 1%, a value largely acceptable for a wide range of process engineering applications, while the deviation is equal to 27% in the SAR1 configuration at the same location.

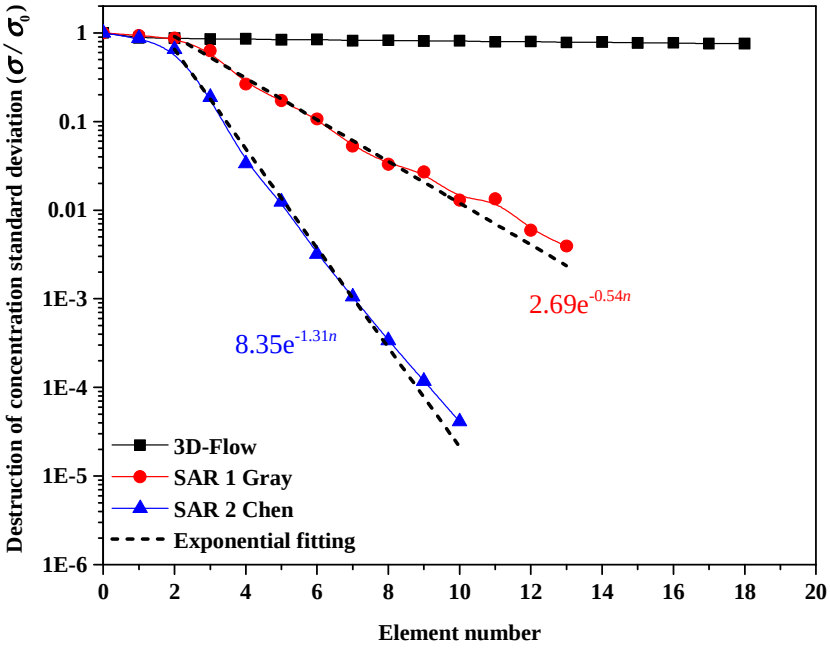

(a)

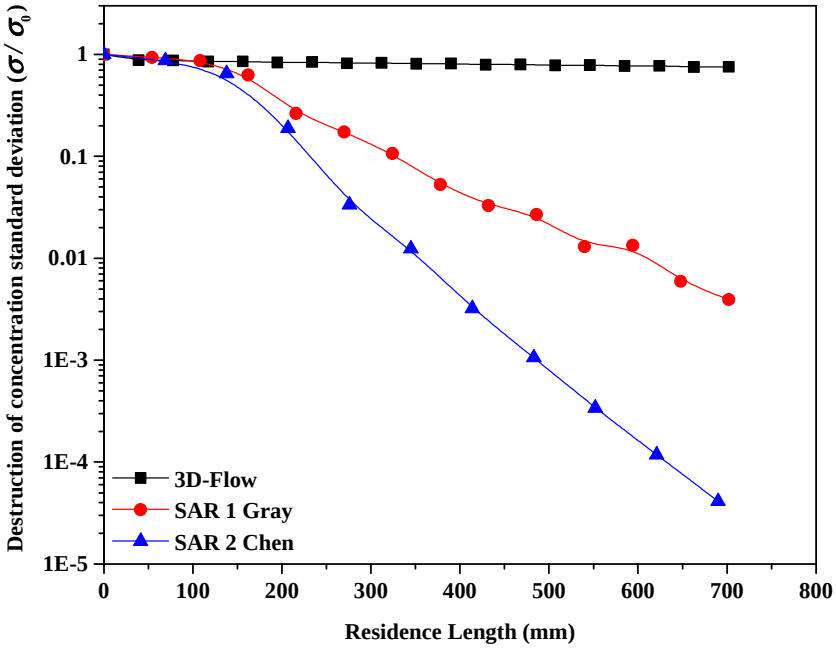

(b)

Figure 6: Normalized scalar standard deviation (a) at the outlet of each element and (b) versus the residence length for the three configurations: 3D-Flow, SAR1, and SAR2

3.4 Pressure losses and friction factors

Figure 7 (a) represents the normalized pressure drop between the inlet and the outlet of each mixing element in the three configurations, where Δp_0 corresponds to the pressure drop in the plain duct flow. The seemingly surprising result from this figure is that the pressure drop in the 3D-Flow configuration is larger than that in the SAR configurations and that the relative pressure drop in the latter case is lower than 1. This implies that the pressure losses across the SAR mixing elements are smaller than those in the straight plain duct with the same inlet mean flow velocity. However, the reason behind this behavior is that in the SAR configurations, the flow is divided into two channels of the same cross section, so that the flow rate is divided by 2 in each channel, inducing lower pressure drop as it can be observed from the streamlines colored by the mean flow velocity in Figure 2. Therefore, to account for this issue, it is preferable to compare the friction factors that can scale out the flow rate issue.

The Fanning friction coefficient is obtained from the pressure drop across the mixer inlet and outlet via the following relation:

$$f = \frac{\Delta p D_h}{2L\rho u_m^2} \tag{7}$$

where u_m is the mean flow velocity.

In the straight plain pipe and 3D-Flow configurations, u_m is simply the mean flow velocity, which is uniform throughout the entire mixer length. However, in the SAR configurations, the calculation of the friction coefficient should be weighted by the corresponding flow velocity. In SAR1 configuration, 10% of the flow volume corresponds to a mean flow velocity u_m while 90% corresponds to the half of the mean flow velocity $u_m/2$. In SAR2, the volume corresponding to u_m is 13% while that corresponding to $u_m/2$ is 87%. Let us denote β the fraction of the volume corresponding to $u_m/2$; the friction coefficient would be calculated using the following expression:

$$f_{SAR} = \frac{\Delta p D_h}{2L\rho u_m^2}(1-\beta) + \frac{\Delta p D_h}{2L\rho\left(\frac{u_m}{2}\right)^2}\beta \tag{8}$$

which leads to the following equation:

$$f_{SAR} = \frac{\Delta p D_h}{2L\rho u_m^2}(1 + 3\beta) \quad (9)$$

The normalized friction coefficients are shown in Figure 7 (b) where f_0 corresponds to the fiction coefficient of the plain duct flow. The friction ratios are greater than 1, since the losses in straight duct are always the lowest. Moreover, the friction in the 3D-Flow configuration is smaller than in the SAR configurations due to smaller number of bends. The increase in the friction losses in the 3D-Flow relative to the straight duct is about 11%, while it is larger in the SAR cases: SAR1 has an increase of about 65% and SAR2 has an increase of about 68%, which is quite similar although slightly higher than SAR1 configuration.

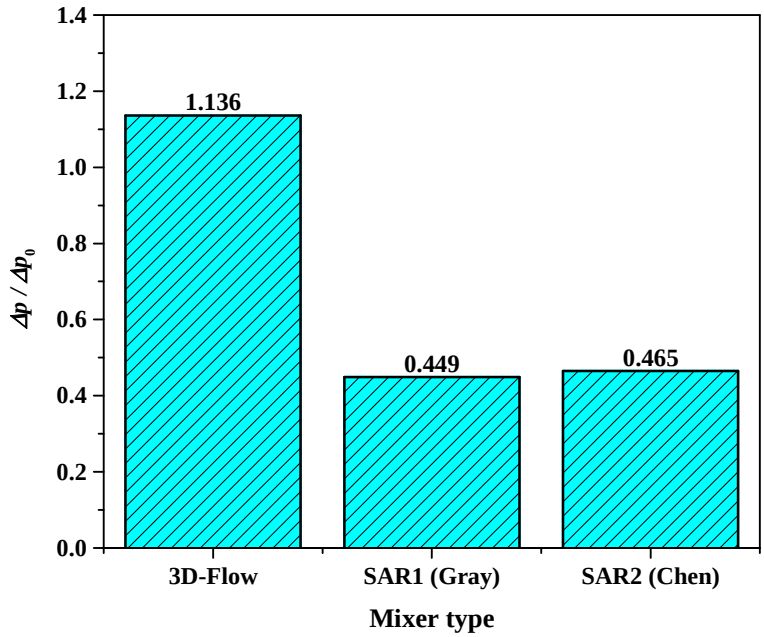

(a)

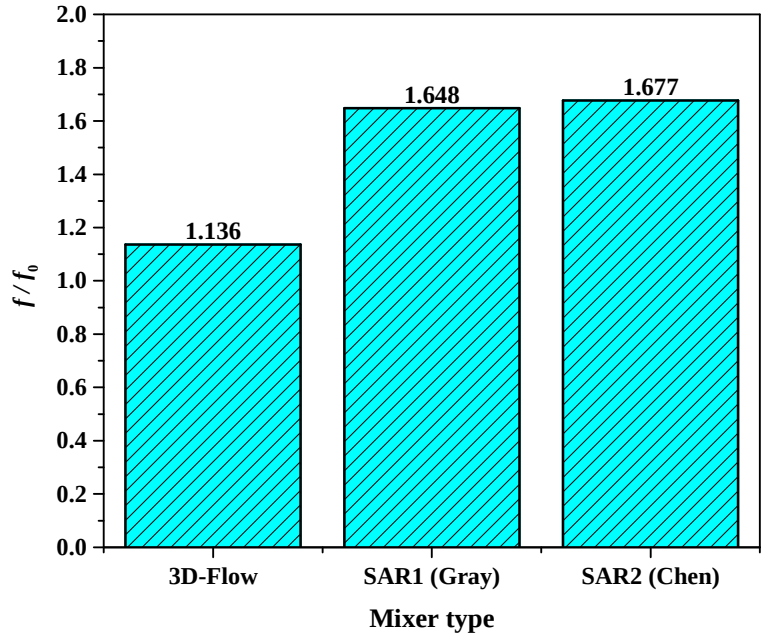

(b)

Figure 7: (a) Normalized pressure drop and (b) normalized Fanning friction coefficient for the three configurations: 3D-Flow, SAR1, and SAR2

3.5 Relative mixing efficiency

An alternative way of assessing the mixing performance is by comparing the relative mixing efficiency of the different configurations at constant pumping power. The relative mixing efficiency is defined as the relative difference in the standard deviations between the mixer and that of a straight duct at constant pumping power:

$$\eta = \left.\frac{\sigma_0 - \sigma}{\sigma_0}\right|_{pp} \tag{10}$$

For equal pumping power:

$$\dot{V}_0 \Delta p_0 = \dot{V} \Delta p \tag{11}$$

where $\dot{V}$ is the volumetric flow rate.

Substituting Δp by an expression in terms of f and substituting $\dot{V}$ by an expression in terms of Reynolds number Re, it follows that:

$$\frac{Re}{Re_0} = \left(\frac{f}{f_0}\right)^{-\frac{1}{3}} \tag{12}$$

Thus at constant pumping power, the relative mixing efficiency becomes:

$$\eta = \left(\frac{\sigma_0 - \sigma}{\sigma_0}\right)\left(\frac{f}{f_0}\right)^{-\frac{1}{3}} \tag{13}$$

Figure 8 represents the variation of the relative mixing efficiency versus the residence length for the three different configurations. The SAR2 geometry has higher relative mixing efficiency than SAR1 and 3D-Flow configurations. In the 3D-Flow, the efficiency increases very slowly to reach a maximum value of about 22% at the mixer exit since the mixing in this configuration is almost entirely due to molecular diffusion. In the SAR configurations, the efficiency increases rapidly to reach a plateau after about 300 mm from the inlet. The maximum efficiency in SAR1 and SAR2 geometries is almost the same; it is around 83%. However, mixing increases faster in the SAR2 compared to SAR1.

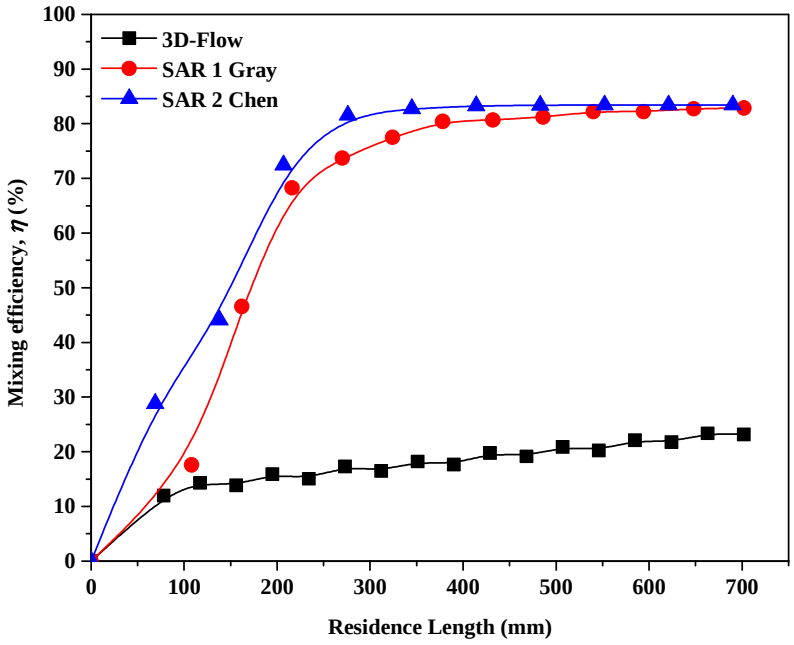

Figure 8: Relative mixing efficiency versus the residence length in the three configurations: 3D-Flow, SAR1, and SAR2

4 Conclusions

Mixing quality in chaotic flux recombination reactors is numerically investigated. The split/recombination mechanism is a practical realization of the mathematical baker's transform that generates chaotic structures and exponentially increases the interfacial area between fluid layers. This process significantly promotes mixing by molecular diffusion. Between two subsequent split and recombination phases, several rotations and flow direction changes are passively imposed on the flow contributing to the continuous stretching and folding of the viscous fluid.

The studied compact SAR configurations (SAR1 and SAR2), first proposed by Gray *et al.* [2] and Chen and Meiners [3] respectively, are reproduced on a milli-scale exploitable in the industrial applications of handling viscous fluids and deeply laminar flows. A three-dimensional flow configuration with no split/recombination (3D-Flow) is also studied in terms of relative mixing efficiency and pressure drop, the baseline geometry being a plain square channel.

The governing momentum and passive scalar conservation equations are solved using a Eulerian approach and a finite volume method with the SIMPLE algorithm for pressure-velocity coupling.

As the flow is deeply laminar and the fluid is highly viscous, the 3D-Flow configuration shows little mixing enhancement with respect to plain pipe flow and generates a higher pressure drop. The flux recombination mixers however, show an interesting rapid decrease in scalar concentration gradients. In SAR2 configuration, for example, the normalized scalar concentration standard deviation from the mean attains values as low as 1% as early as at the inlet of the fifth element. At the same location, those for SAR1 geometry are calculated at 27%. Indeed, SAR2 mixer shows superior mixing performance compared to the other configurations. The Poincaré sections, produced by releasing inert particles at the inlet and following their paths through the mixer outlet, show the capacity of SAR configurations to generate chaotic-type behavior in laminar flow. Particles remain grouped in plain pipe and 3D-flow while they get dispersed and visit several locations in the cross-section of the SAR configurations, especially in SAR2 mixer, confirming the conclusions based on scalar standard deviation values.

To properly evaluate the interest of these devices in process industry, energy expenditures behind the mixing enhancement are evaluated in terms of pressure drop. For similar inlet Reynolds number, SAR mixers generate lower pressure drops than 3D-Flow and the plain channel due to the fact that the fluid flows in the majority of their volume with half of the inlet velocity due to splitting, thus decreasing head losses. To account for this point, the normalized non-dimensional longitudinal Fanning friction coefficient is calculated and compared: 3D-Flow shows values 11% increase compared to the plain channel; the increase in SAR1 and SAR2 mixers being 65% and 68% respectively.

Mixing performance and energy consumption are simultaneously evaluated in the relative mixing efficiency parameter which gives the relative increase in mixing quality with respect to a plain square channel at constant pumping power. While the maximum efficiency in 3D-Flow remains limited to 22%, SAR1 and SAR2 configurations show values as high as 83% with the SAR2 mixer finally manifesting the fastest mixing rates, dissipating concentration gradients with minimal residence time and moderate pressure drops.

In this context, the numerical simulations offer a powerful design and optimization tool giving insight to the optimal number of elements as a compromise between product quality and energy expenditures.

Acknowledgments

C. Habchi and T. Lemenand would like to thank the PHC CEDRE program and the Research Commission of Angers University for the grants allowing researcher exchange between France and Lebanon. The authors dedicate this work to their dear colleague Philippe Carrière, senior scientist in the CNRS, deceased in February 2015. Among many other contributions, he has introduced us to the art of the baker's transform, in the framework of the Energy Program 2006 AC PR1-2-22.

References

[1] P.E. Neerincx, R.P.J. Denteneer, S. Peelen, H.E.H. Meijer, Compact Mixing Using Multiple Splitting, Stretching, and Recombining Flows, Macromolecular Materials and Engineering 296 (2011) 349-361.

[2] B.L. Gray, D. Jaeggi, N.J. Mourlas, B.P.v. Drieenhuizen, K.R. Williams, N.I. Maluf, G.T.A. Kovacs, Novel interconnection technologies for integrated microfluidic systems, Sensors and Actuators 77 (1999) 57-65.

[3] H. Chen, J.-C. Meiners, Topologic mixing on a microfluidic chip, Applied Physics Letters 84 (2004) 2193-2195.

[4] M. Jarrahi, J.P. Thermeau, H. Peerhossaini, Heat transfer enhancement in split and recombine flow configurations: A numerical and experimental study, ASME, FEDSM, Washington, DC, USA, 2016.

[5] Y. Hirata, K. Ohkawa, Development of Channel Mixers Utilising 180° Fluid Rotation Combined with Split and Recombination, Chemical Engineering Research and Design 108 (2016) 118-125.

[6] P. Carriere, On a three-dimensional implementation of the baker's transformation, Physics of Fluids 19 (2007) 118110-118114.

[7] A. Ghanem, T. Lemenand, D. Della Valle, H. Peerhossaini, Static mixers: Mechanisms, applications, and characterization methods – A review, Chemical Engineering Research and Design 92 (2014) 205-228.

[8] S. Hossain, K.-Y. Kim, Mixing analysis in a three-dimensional serpentine split-and-recombine micromixer, Chemical Engineering Research and Design 100 (2015) 95-103.

[9] A. Ghanem, T. Lemenand, D. Della Valle, H. Peerhossaini, Optimized chaotic heat exchanger configurations for process industry: A numerical study, ASME, FEDSM,Incline Village, Nevada, USA, 2013.

[10] M. Creyssels, S. Prigent, Y. Zhou, X. Jianjin, C. Nicot, P. Carrière, Laminar heat transfer in the “MLLM” static mixer, International Journal of Heat and Mass Transfer 81 (2015) 774-783.

[11] M.A. Ansari, K.-Y. Kim, Mixing performance of unbalanced split and recombine micomixers with circular and rhombic sub-channels, Chemical Engineering Journal 162 (2010) 760-767.

[12] J.J. Chen, C.H. Chen, S.R. Shie, Optimal designs of staggered dean vortex micromixers, International journal of molecular sciences 12 (2011) 3500-3524.

[13] Z. Anxionnaz-Minvielle, P. Tochon, R. Couturier, C. Magallon, F. Théron, M. Cabassud, C. Gourdon, Implementation of ‘chaotic’ advection for viscous fluids in heat exchanger/reactors, Chemical Engineering and Processing: Process Intensification 113 (2017) 118-127.

[14] A. Ghanem, T. Lemenand, D. Della Valle, H. Peerhossaini, Transport phenomena in passively manipulated chaotic flows: Split-and-recombine reactors, ASME, FEDSM,Incline Village, Nevada, USA, 2013.

[15] ANSYS, Fluent, Academic Research, version 15.

[16] R.F. Warming, R.M. Beam, Upwind second-order difference schemes and applications in aerodynamic flows, AIAA Journal 14 (1976) 1241-1249.

[17] J.T. Barth, D. Jespersen, The design and application of upwind schemes on unstructured meshes, AIAA 27th Aerospace Sciences Meeting Reno, Nevada, 1989.

[18] S. Patankar, Numerical Heat Transfer and Fluid Flow, Hemisphere Publishing Co., New York, 1980.

[19] R.K. Thakur, C. Vial, K.D.P. Nigam, E.B. Nauman, G. Djelveh, Static Mixers in the Process Industries—A Review Chemical Engineering Research and Design 81 (2003) 787-826.

[20] I.B. Celik, U. Ghia, P.J. Roache, C.J. Freitas, H. Coleman, P.E. Raad, Procedure for Estimation and Reporting of Uncertainty Due to Discretization in CFD Applications, Journal of Fluids Engineering 130 (2008) 078001-078001.

[21] S.S. Soman, C.M.R. Madhuranthakam, Effects of internal geometry modifications on the dispersive and distributive mixing in static mixers, Chemical Engineering and Processing: Process Intensification 122 (2017) 31-43.

[22] C. Park, J. Lee, H. Cho, Y. Kim, S. Cho, I. Moon, Strategies for evaluating distributive mixing of multimodal Lagrangian particles with novel bimodal bin count variance, Powder Technology 325 (2018) 687-697.